System Model and Performance Evaluation of Single-Stage Buck-Boost Type Manitoba Inverter for PV Applications

Ken K.M. Siu, *Student Member, IEEE,* and Carl N.M. Ho, *Senior Member, IEEE*

***Abstract*--The paper presents a control methodology for a recently proposed single-stage buck-boost type inverter in photovoltaic (PV) applications. A wide range of input voltage is covered and the dc power is effectively converted into the grid power within a single-stage system. However, from the topological characteristics, a CL filter is always formed at the system output which results in a resonance pole in the control system. In the PV system, the panel output voltage keeps varying. Under the traditional control method, stability issues may occur, which poses a challenge to controller design. Thus, targeting on PV applications, a comprehensive control methodology is presented in this paper. Under such control scheme, a high quality ac grid power is guaranteed and the power conversion maintains in a stable manner. Meanwhile, the maximum power point (MPP) of PV panels is always tracked and no additional current sensor is required in the maximum power point tracking (MPPT) design. In this paper, a detailed system analysis is presented which includes the system modelling and the stability evaluation. The performance of the presented control methodology is experimentally verified in a 750 W PV inverter platform. Both steady state and dynamic characteristics are in good agreement with theoretical knowledge.**

***Index Terms*-- Maximum power point tracking, photovoltaic inverter, single-stage buck-boost.**

I. Introduction

RECENTLY, solar energy becomes one of the important renewable energy sources in the world which is environmentally friendly and is replenished constantly in nature. With the use of photovoltaic (PV) inverters [2], [3], solar power is able to be effectively transferred from the PV panels to the power grid. The generated power is used to support the power demand in those localized areas, such as residential usages, solar farms and industrial applications. Generally, the basic requirements for PV inverters are to achieve highly efficient power conversion, low design cost, and low leakage current. Thus, in order to simplify the structure of the two-stage system and to achieve an efficient power transmission, many single-stage PV inverter solutions, [4] - [7], have recently been proposed.

A buck-boost type transformerless inverter is proposed in [7], in which the low voltage dc power is able to be converted into ac grid power within a single-stage system. The topology

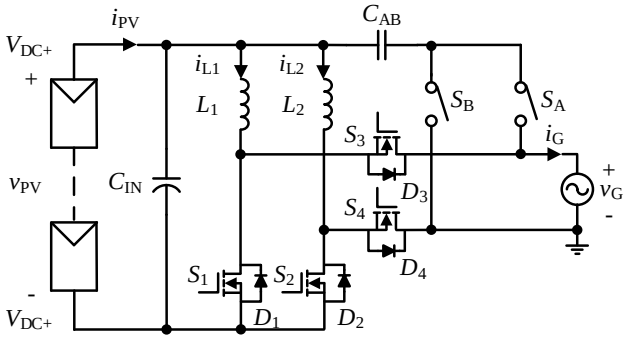

Fig. 1. Single-stage buck-boost type inverter.

is named as Manitoba Inverter and is shown in Fig. 1. Based on the topological characteristics, a *CL* filter is always formed at the inverter output which is similar to other buck-boost type inverters connected to an external *CL* filter. A continuous grid current is guaranteed and the system leakage current is minimized. However, a phase shift property and a resonance characteristic have been generated. In PV applications, the panel output remains varied under different environmental conditions and even transient steps may occur. Therefore, the resonance characteristic has generated a great impact on system stability, which makes the design of the system control to become more challenging. To maintain a stable performance of a PV inverter system, varying types of methodologies were presented in the past. In [8], simple PI control is applied. In the control scheme, both input and output voltage information are always required to calibrate the difference between the buck-boost inductor current and the output current. Therefore, the accuracy of the control is highly dependent on the system parameters. In [9], the control method is based on an averaged continuous-time model and a feedforward compensation. In fact, the compensation circuit helps to eliminate the influence of both input and output voltages and allows the system to be more robust. However, when the system output filter is modified to a *CL* filter, a more complicated average model is resultant. In [10] and [11], one cycle control is adopted into the single-state buck-boost type inverter to offer a fast dynamic system response. The control structure is simple and no PLL is required, but, the possible filter resonance issue cannot be compensated in the control and may cause stability problems. In [12] and [13], sliding mode control is applied to PV inverter

The work described in this paper was supported by a grant from Canada Research Chairs, Canada (Sponsor ID: 950-230361). Part of the work described in this paper has been presented in the ECCE2018. [1]

Ken K.M. Siu, (Corresponding author), and Carl N.M. Ho are with the RIGA Lab, the Department of Electrical & Computer Engineering, University of Manitoba, R3T5V6, Winnipeg, MB, Canada (E-mail: siukm3@myumanitoba.ca).

which is another type of non-linear control method. Stable performance and good dynamic response can be obtained. The determination of the sliding surface is based on the state equation of the inverter. So when the output filter order is higher, the calculation of the switching criteria becomes more complicated. In the reviewed papers, they are not grid-connected control, which is with a resistive load and is paralleled with a capacitor. A continuous current always results at the load. However, for grid-connected applications, an output filter is required as the large discontinuous current will not be accepted in the industry. Due to an additional *CL* filter is presented at the output, a resonance characteristic is produced and the system structure is different. To achieve grid-side current control, the controller target also needs to be shifted from the power inductor to the filter inductor, which is also totally different from the reviewed solutions. Therefore, in order to support the stability performance of PV applications at a wide range of system operating points, a different control scheme is required.

A comprehensive control scheme is proposed in this paper to fulfill the high quality grid current and the system stability requirement in a single-stage buck-boost type PV inverter, which is the extension of the work in [1]. The proposed control scheme is focused on PV application and is used to transfer the maximum PV power into the grid power within a single-stage buck-boost type transformerless converter. In contrast to [7], 1) an active damping circuit is designed in the controller to cover a wide range of PV panel voltage instead of a single dc voltage point optimization; 2) Differently, a maximum power point tracking (MPPT) function is integrated in the system as a comprehensive control scheme and the trade-off between the static and dynamic MPPT efficiencies are studied and discussed; 3) In the system design, both inverter and solar source performances are considered instead of just care about the inverter performance.

The proposed control scheme focuses on PV systems, especially those with fixed installation points. A precise switching action and a high quality grid current waveform are produced by the current controls in the middle loop and the inner loop. An active damping circuit, [14], is integrated into the inner loop of the system by using the high frequency (HF) voltage ripple information of the filter capacitor. It helps to erase the filter resonant pole, and the resulting system is able to adopt all the possible voltage inputs. The outer loop is targeted on input voltage which is applied to lock the MPP voltage of the PV panel. A perturb and observe (P&O) method is adopted in the system outer loop and offers the MPPT [15] - [16] function. In the implementation, the system output power is applied to the MPPT as a power reference, thus, no additional current sensor is required at the input of the inverter. Furthermore, both dynamic and steady state characteristics are determined and are applied to optimize the control system design. A 750W inverter platform has been implemented to verify the control theory. All the time, the MPP was tracked and stable performance was guaranteed in both steady state and dynamic situations. All of the experimental results and the detailed findings were consistent with the theoretical analysis.

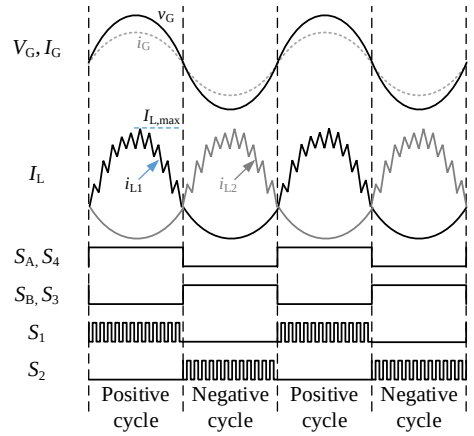

Fig. 2. Gate signals sequence of the buck-boost inverter.

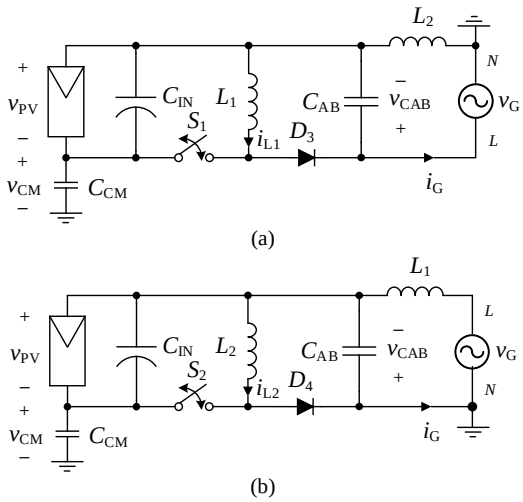

Fig. 3. Equivalent circuit of (a) positive and (b) negative half line cycles.

II. System Configuration

A. Review of Manitoba Inverter

Manitoba inverter is a single-stage buck-boost type inverter system which is in a simple circuit structure. Every half line cycle, the operation of the inverter is able to be converted back to a simple buck-boost type converter circuit. The corresponding modulation scheme of Manitoba Inverter is documented in [7] and is shown in Fig. 2. Accordingly, the equivalent circuits of the inverter connecting to a PV array in the positive and negative half line cycles are found, and are shown in Fig. 3 (a) and (b), respectively.

In each half line cycle, there is only one semiconductor is operated at HF switching and the others are in line frequency (LF) operation. During the power conversion, only two semiconductors are involved in the main current path. So an efficient energy conversion is resultant. From the inverter topology, a reconfigurable *CL* filter is always located at the inverter output side. One of the inductors acts as the grid-side filter inductor and the other one acts as the converter-side power inductor. The roles of the inductor are interchanged in every half line cycle. The *CL* filter is formed by the grid-side inductor and a filter capacitor C_{AB}. Accordingly, in the buck-boost circuit, the discontinuous output current is filtered out and a low noise continuous grid current, i_G, is guaranteed. Moreover, the filter capacitor helps to claim the voltage ripple between the

positive PV terminal and one end of the grid terminal. Thus, the system common mode voltage noise is minimized. So a low noise system is guaranteed which has been reported in [7].

During the positive half line cycle, the buck-boost switching cell is formed by switch S_1, antiparallel diode of D_3 and inductor L_1. S_1 is the only HF switch at this cycle. Switches S_4 and S_A are in LF operation. Both of them are kept ON at this state. S_4 is used to generate a current return path for the circuit and S_A is used to link up the connection between the filter capacitor and the Line terminal of the grid. L_2 inductor acts as the grid-side filter inductor and L_1 acts as the converter-side power inductor. An output *CL* filter is formed by C_{AB} and L_2.

Similarly, during the negative half line cycle, the buck-boost switching cell is formed by switch S_2, antiparallel diode of D_4 and inductor L_2. S_2 is the only HF switch at this cycle. Switches S_3 and S_B are in LF operation. Both of them are kept ON at this state. S_3 is used to generate a current return path for the circuit and S_B is used to link up the connection between the filter capacitor and the Neutral terminal of the grid. L_1 inductor acts as the grid-side filter inductor and L_2 acts as the converter-side power inductor. An output *CL* filter is formed by C_{AB} and L_1.

B. Proposed Control Methodology

Targeted on a single-stage buck-boost type PV inverter system, a comprehensive control is proposed. A block diagram of the corresponding control method is shown in Fig. 4. In the design, the outer loop is a PV voltage control loop that is integrated with an MPPT controller. So that the inverter input is always regulated to the MPP. The middle one is a grid-side current control which is applied to maintain the quality of the inverter output current. The inner one is an inductor-side current control plus an active damping circuit. It is used to handle the power conversion on the system. On the controller implementation, a set of voltage sensors is applied to the system which is used to sense the PV output voltage, v_{PV}, the grid voltage, v_G, and the filter capacitor voltage, v_C. In addition, a set of current sensors is required which is used to sense the inductor currents, i_{L1} and i_{L2}.

In the outer loop, it is a PV output voltage control which is combined by a simple proportional integral (PI) control and an MPPT method. The control reference in the outer loop is generated from the MPPT function. A P&O method is adopted in the design where the inverter output power and PV voltage are used to track the MPP from the non-linear characteristic of PV panel. A small voltage step is given in every tracking process. If the increment of the average power is in the same direction as the given voltage step, then another voltage step is given until the power level falls or remains stable. As the inverter output power is applied to the MPPT block, no extra current sensor is required on the system design. The corresponding program flow is shown in Fig. 5. Based on the reference voltage from the P&O, a simple PI control is applied to regulate the inverter input to the MPP. Thus, all the time, the maximum power is extracted from the PV panel and the inverter system is kept with a stable input. The output of the voltage control is a grid-side current reference, $i_{G,ref}$, which is the input of the middle loop of the system.

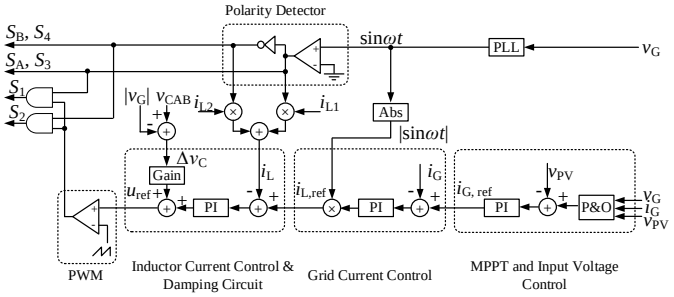

Fig. 4. Block diagram of the presented control methodology.

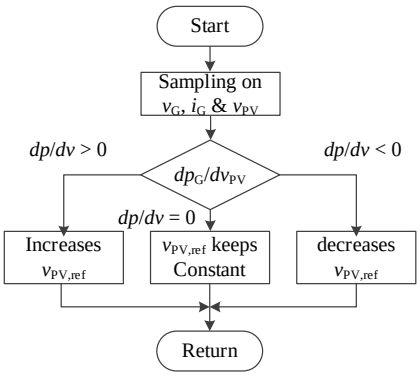

Fig. 5. Logic flow of P&O control block.

In the middle and the inner loops of the system, a double current control method is applied where both grid-side and converter-side inductor currents are under controlled. The grid-side inductor current is controlled through the middle loop and the converter-side inductor current is controlled by the inner loop. The grid-side and converter-side current information are able to be generated from the two inductor current sensors. The roles of both inductors are interchanged in every half line cycle. Therefore, by combining current information in i_{L2} at the positive half line cycle and the current information in i_{L1} at the negative half line cycle, the grid-side current information is generated. Similarly, through the current information in i_{L1} at the positive half line cycle and the current information in i_{L2} at the negative half line cycle, the converter-side current information is generated. The detail is shown in Fig. 4 and the corresponding waveform is shown in Fig. 2. The middle loop is a grid-side current control which is implemented by a PI control. It is used to compensate the phase shift generated by the *CL* filter and to control the power factor of the system output close to one. Thus, a high quality output waveform is resultant. The output of the middle loop is a converter-side inductor current reference, $i_{L,ref}$, which is the input of the inner loop.

The inner loop is a converter-side inductor current control which is used to offer a precise switching action for the inverter and to avoid the filter resonance in the system. Based on the system operation, a resonant pole is created by the *CL* filter. In a general fixed input voltage design, the stability issue that generated from the resonant pole can be avoided through a careful design in the system control bandwidth. However, in a condition is always varying with time. Thus, system stability becomes challenging to ensure. In the design, an active damping circuit is integrated into the PI current control loop PV system, the panel output is non-linear and the system where the

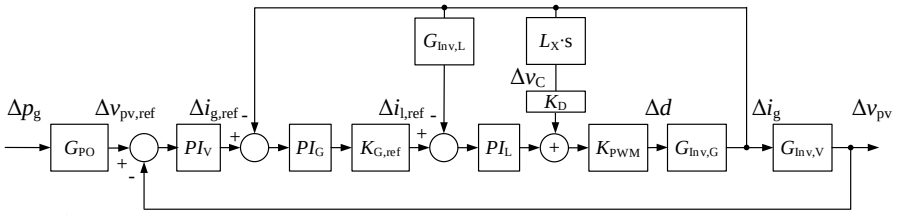

Fig. 6. Controller small signal flow diagram.

capacitor ripple voltage is applied as a damping factor [14]. Accordingly, its performance is similar to a resistor virtually series connecting to the converter-side inductor. The output of the converter-side inductor current control loop is a duty cycle reference, u_{ref}. Through the comparison with the sawtooth signal, the control signals of the HF switch are generated. All the time, only one switch is under HF operation and the others are in LF operation. The whole controller design is maintained in a simple structure.

In the reconfigurable filter circuit, the switching action of S_A and S_B are controlled by a polarity detection circuit. By sensing the signal of v_G, S_A and S_B are switched alternatively and are synchronized with LF operation. In the positive half line cycle, S_A is conducted and S_B is off. In contrast, on the negative half line cycle, the switching action is opposite. Thus, during the system operation, a *CL* filter is always formed at the inverter output. At the same time, the grid current remains continuous and has a low current ripple on top.

III. System Modelling

A. Review of PV Panel Model

The overall system model can be separated into two parts, which are the modelling of PV panel and the modelling of inverter system. Referring to [17], a single diode equivalent circuit is applied to simulate the performance of a PV panel. The characteristic of PV panel is modelled as,

$$I_{PV} = I_{ph} - I_0 \cdot \left(e^{\frac{V_{PV}+I_{PV}\cdot R_S}{N_S \cdot V_T}} - 1 \right) - \frac{V_{PV}+I_{PV}\cdot R_S}{R_{SH}}, \quad (1)$$

where I_{PV} is current of panel output, I_{ph} is photogenerated current, I_0 is diode saturation current, N_s is number of series cell, R_{SH} is the shunt resistance in the PV model, R_S is the series resistance in the PV model and V_T is temperature coefficient.

Through Lambert function [18], (1) is reformulated to,

$$I_{PV} = \frac{R_{TH}}{R_S} \cdot \left(I_{TH} - \frac{V_{PV}}{R_{SH}} \right) - \frac{N_S \cdot V_T}{R_S} \cdot W\left(\frac{I_0 \cdot R_{TH}}{N_S \cdot V_T} \cdot e^{\frac{1}{N_S \cdot V_T}\left[V_{PV} \cdot \left(1 - \frac{R_{TH}}{R_{SH}} \right) + I_{TH} \cdot R_{TH} \right]} \right), \quad (2)$$

where I_{TH} equals $I_{ph} + I_0$ and R_{TH} equals $\frac{R_{SH}\cdot R_S}{R_{SH}+R_S}$.

As shown in (1) and (2), the PV panel output characteristic is in a non-linear behavior and is depended on the sun radiation and environment temperature. Referred to the PV simulator characteristic, the corresponding series and shunt resistances are 0.81 ohms and 410 ohms, respectively.

B. Inverter System Model

The applied inverter is a single stage system. It has a symmetrical system structure in the positive and the negative half line cycles. Thus, with the used of positive half line cycle information is sufficient to develop the whole converter system model. In the positive line cycle, L_2 acts as a grid-side inductor which handles the grid current, i_G. In addition, L_1 becomes the converter-side inductor and the current flowing on top is defined as i_L. In the design, all the inductors are set to the same value. Such that L_1 is equal to L_2 and is grouped as L_X.

As shown in Fig. 3 (a), when S_1 is ON, the converter-side inductor is charging. When S_2 is OFF, the energy in the converter-side inductor is transferred to the grid. By combining the on-state and the off-state system conditions, a set of state-space averaging equations is formed and is shown as,

$$\frac{d}{dt}\begin{bmatrix} i_L \\ i_G \\ v_{pv} \\ v_{CAB} \end{bmatrix} = \begin{bmatrix} 0 & 0 & \frac{D}{L_X} & -\frac{1-D}{L_X} \\ 0 & 0 & 0 & \frac{1}{L_X} \\ -\frac{D}{C_{IN}} & 0 & 0 & 0 \\ \frac{1-D}{C_{AB}} & -\frac{1}{C_{AB}} & 0 & 0 \end{bmatrix} \begin{bmatrix} i_L \\ i_G \\ v_{pv} \\ v_{CAB} \end{bmatrix} + \begin{bmatrix} 0 \\ -\frac{v_G}{L_X} \\ \frac{i_{pv}}{C_{IN}} \\ 0 \end{bmatrix}, \quad (3)$$

where D is duty cycle of the system.

C. System Small Signal Model

In the system stability evaluation, small signal analysis method is applied. From Fig. 4, a corresponding small signal model of the system is determined and is given in Fig. 6.

From the PV panel portion, by considering $\Delta v_{pv}(t)$ and $\Delta i_{pv}(t)$ as the small-signal perturbations of v_{pv} and i_{pv} in the small signal analysis model, (1) is rearranged. Through small signal approximation method, [19], the small-signal perturbation equation of the PV characteristic is found as,

$$\Delta i_{pv} = -\frac{\frac{I_0}{N_S \cdot V_T} \cdot e^{\frac{V_{PV}+I_{PV}\cdot R_S}{N_S \cdot V_T}}}{1 + \frac{R_S}{R_{SH}} + \frac{I_0 \cdot R_S}{N_S \cdot V_T} \cdot e^{\frac{V_{PV}+I_{PV}\cdot R_S}{N_S \cdot V_T}}} \cdot \Delta v_{pv} = -X_{PV} \cdot \Delta v_{pv}, \quad (4)$$

where X_{PV} is defined as $\frac{\frac{I_0}{N_S \cdot V_T} \cdot e^{\frac{V_{PV}+I_{PV}\cdot R_S}{N_S \cdot V_T}}}{1 + \frac{R_S}{R_{SH}} + \frac{I_0 \cdot R_S}{N_S \cdot V_T} \cdot e^{\frac{V_{PV}+I_{PV}\cdot R_S}{N_S \cdot V_T}}}$.

As shown in (2), Δv_{pv} is directly proportional to Δi_{pv} which is matched with the PV characteristic curve.

From the inverter system portion, by considering $\Delta v_{CAB}(t)$, $\Delta v_{pv}(t)$, $\Delta i_l(t)$, $\Delta i_g(t)$ and Δd as the small-signal perturbations of v_{CAB}, v_{pv}, i_L, i_G and D respectively in the small signal analysis model, (3) is able to be rearranged into a set of small-signal perturbations equations, (5) – (8), as,

$$L_X \cdot s \cdot \Delta i_l = (V_{PV} + V_{CAB}) \cdot \Delta d + D \cdot \Delta v_{pv} - D' \cdot \Delta v_{CAB}, \quad (5)$$

$$L_X \cdot s \cdot \Delta i_g = \Delta v_{CAB}, \quad (6)$$

$$C_{IN} \cdot s \cdot \Delta v_{pv} = -X_{PV} \cdot \Delta v_{pv} - i_L \cdot \Delta d - D \cdot \Delta i_l, \quad (7)$$

$$C_{AB} \cdot s \cdot \Delta v_{CAB} = D' \cdot \Delta i_l - i_L \cdot \Delta d - \Delta i_g, \quad (8)$$

where $D' = 1 - D$.

From (4), (5) – (8), the relationship of the inverter is able to found. In the derivation, the influence of Δi_{pv} can be eliminated as the scale of X_{PV} is relatively small compared to other parameters. The converter models are developed as,

$$G_{\mathrm{inv,L}}(s) = \frac{C_{\mathrm{AB}} \cdot C_{\mathrm{IN}} \cdot L_2 \cdot V_{\mathrm{X}} \cdot s^3 + L_{\mathrm{X}} \cdot (I_{\mathrm{G}} \cdot C_{\mathrm{IN}} - I_{\mathrm{PV}} \cdot C_{\mathrm{AB}}) s^2 + V_{\mathrm{X}} \cdot C_{\mathrm{IN}} \cdot s - I_{\mathrm{PV}}}{-C_{\mathrm{IN}} \cdot L_2 \cdot I_{\mathrm{PV}} / D \cdot s^2 + V_{\mathrm{X}} \cdot C_{\mathrm{IN}} \cdot D' \cdot s - I_{\mathrm{PV}}}, \quad (9)$$

$$G_{\mathrm{inv,G}}(s) = \frac{-C_{\mathrm{IN}} \cdot L_2 \cdot I_{\mathrm{PV}} / D \cdot s^2 + V_{\mathrm{X}} \cdot C_{\mathrm{IN}} \cdot D' \cdot s - I_{\mathrm{PV}}}{C_{\mathrm{AB}} \cdot C_{\mathrm{IN}} \cdot {L_{\mathrm{x}}}^2 \cdot s^4 + L_{\mathrm{X}} \cdot (C_{\mathrm{IN}} + D^2 \cdot C_{\mathrm{AB}} + D'^2 \cdot C_{\mathrm{IN}}) s^2 + D^2}, \quad (10)$$

where V_{X} equals to sum of dc and ac voltage.

As shown in (9) and (10), since the presence of a filter capacitor and a grid-side inductor, more pole and zero are added into the system. A resonant point is induced and it makes the controller design to be challenging.

In the proposed control methodology, an active damping is inserted into the inner loop of the system. The capacitor ripple voltage is applied as the damping factor. K_{D} is the damping coefficient. In the inner loop, considering the effect of the damping system, the relationship between the duty ratio and the converter-side inductor current, $G_{\mathrm{inv,D}}$, is found as,

$$G_{\mathrm{inv,D}}(s) = \frac{\Delta i_{\mathrm{l}}}{\Delta d} = \frac{G_{\mathrm{inv,L}}(s) \cdot G_{\mathrm{inv,G}}(s)}{1 - K_{\mathrm{D}} . K_{\mathrm{PWM}} . L_{\mathrm{X}} . s . G_{\mathrm{inv,G}}(s)}, \quad (11)$$

which is rearranged to (12).

From (12), it shows that the effect of the active damping circuit is concentrated on the denominator of the transfer function. With the help of the active damping circuit, the influence from the resonance characteristic is eliminated. Through the Routh-Hurwitz stability criterion, the range of the damping ratio, K_{D}, is given as,

$$0 < K_{\mathrm{D}} < \frac{(1 + D'^2) \cdot C_{\mathrm{IN}} + D^2 \cdot C_{\mathrm{AB}}}{K_{\mathrm{PWM}} . V_{\mathrm{X}} \cdot C_{\mathrm{IN}} \cdot D'}. \quad (13)$$

For overall transfer function of the system inner loop is calculated as,

$$G_{\mathrm{inner}}(s) = K_{\mathrm{PWM}} . G_{\mathrm{inv,D}}(s) . PI_{\mathrm{L}}(s). \quad (14)$$

Accordingly, the overall transfer function of the system middle loop is formed as,

$$G_{\mathrm{middle}}(s) = \frac{G_{\mathrm{inner}}(s)}{G_{\mathrm{inv,L}}(s) \cdot (1 + G_{\mathrm{inner}}(s))} \cdot K_{\mathrm{G,ref}} \cdot PI_{\mathrm{G}}(s). \quad (15)$$

For the outer loop model, the system power equation is applied and is listed as,

$$p_{\mathrm{PV}} = v_{\mathrm{PV}} \cdot i_{\mathrm{PV}} = \frac{1}{2} \cdot C_{\mathrm{IN}} \frac{d{v_{\mathrm{PV}}}^2}{dt} + v_{\mathrm{G}} \cdot i_{\mathrm{G}}. \quad (16)$$

By considering $\Delta p_{\mathrm{PV}}(t)$, $\Delta v_{\mathrm{PV}}(t)$, $\Delta i_{\mathrm{PV}}(t)$ and $\Delta i_{\mathrm{G}}(t)$ as the small-signal perturbations of p_{pv}, v_{pv}, i_{pv} an i_{G} in the small signal analysis model, the relationship between the input and output sides can be found as,

$$G_{\mathrm{inv,V}}(s) = \frac{\Delta v_{\mathrm{pv}}}{\Delta i_{\mathrm{g}}} = \frac{V_{\mathrm{G}}}{I_{\mathrm{pv}} - X_{\mathrm{pv}} \cdot V_{\mathrm{pv}} - s \cdot C_{\mathrm{IN}} . V_{\mathrm{pv}}}, \quad (17)$$

$$G_{\mathrm{PO}}(s) = \frac{\Delta v_{\mathrm{pv}}}{\Delta p_{\mathrm{g}}} = \frac{1}{I_{\mathrm{pv}} - X_{\mathrm{pv}} \cdot V_{\mathrm{pv}} - s \cdot C_{\mathrm{IN}} . V_{\mathrm{pv}}}. \quad (18)$$

From (18), it shows that the input capacitor dominates the performance of the outer loop. The higher in capacitance value, the lower controller bandwidth is obtained.

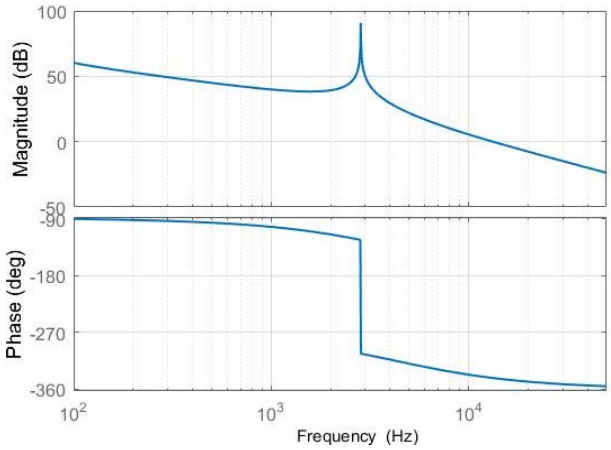

Fig. 7. Bode plot of the relationship between duty cycle and grid current.

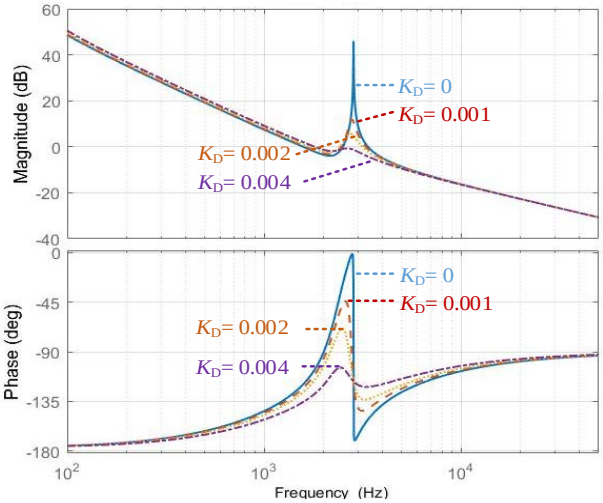

Fig. 8. Bode plot of the inner loop with different damping ratios.

IV. System Performance Evaluation

A. Stability Analysis

From the determined system models, the relationship of each individual loops is found. Thus, the Bode plot is applied to evaluate the system stability. Due to the presence of the *CL* filter in the system, the system stability issue becomes a concern and it increases the difficulty in the controller design. The frequency response of (10) is given in Fig. 7, which represents the system response under a single grid-side current loop control. As shown in the figure, a resonant point appears at 2.8 kHz together with a 180 degree phase change. At that point, a complex resonant pole occurs and the system gain margin point is located. Under traditional PI control method, the system would not meet the stability margin in the plot. Therefore, a different control method is proposed in this paper to handle the new circuit characteristic.

In the presented control strategy, the system inner loop is a converter-side inductor current control and a capacitor voltage damping circuit. The effect of the damping circuit in the inner loop is shown in Fig. 8. When the system doesn't have any damping factor, high resonance peak and large phase change occur at that frequency point. At each operation point, the

$$G_{\mathrm{inv,D}}(s) = \frac{C_{\mathrm{AB}} \cdot C_{\mathrm{IN}} \cdot L_{\mathrm{X}} \cdot V_{\mathrm{X}} \cdot s^3 + L_{\mathrm{X}} \cdot (I_{\mathrm{G}} \cdot C_{\mathrm{IN}} - I_{\mathrm{PV}} \cdot C_{\mathrm{AB}}) s^2 + V_{\mathrm{X}} \cdot C_{\mathrm{IN}} \cdot s - I_{\mathrm{PV}}}{(C_{\mathrm{AB}} \cdot C_{\mathrm{IN}} \cdot {L_{\mathrm{x}}}^2 \cdot s^4 + L_{\mathrm{X}} \cdot (C_{\mathrm{IN}} + D^2 \cdot C_{\mathrm{AB}} + D'^2 \cdot C_{\mathrm{IN}}) s^2 + D^2) + K_{\mathrm{D}} . K_{\mathrm{PWM}} . L_{\mathrm{X}} . s . (C_{\mathrm{IN}} \cdot L_2 \cdot \frac{I_{\mathrm{PV}}}{D} s^2 - V_{\mathrm{X}} \cdot C_{\mathrm{IN}} \cdot D' \cdot s + I_{\mathrm{PV}})}. \quad (12)$$

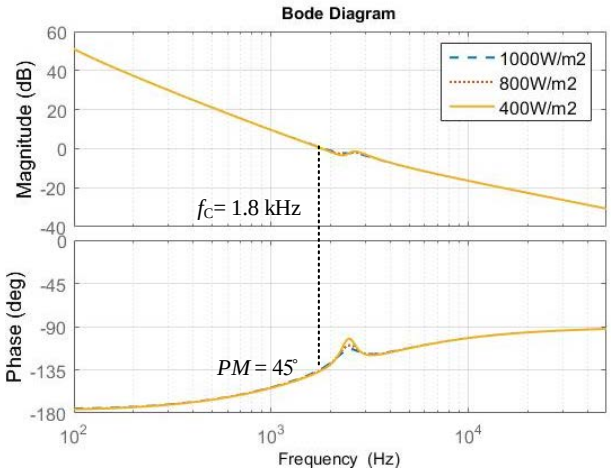

(a)

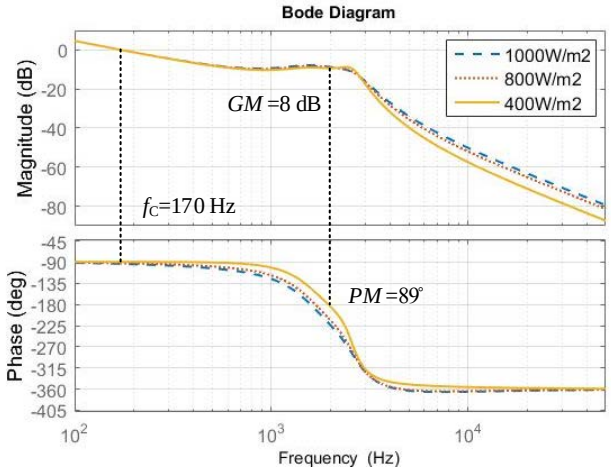

(b)

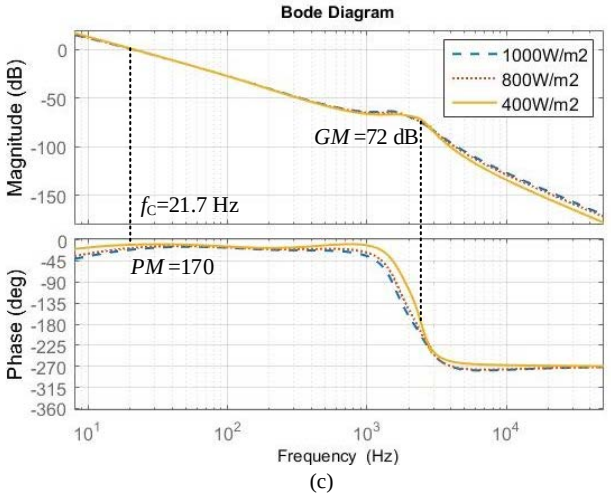

(c)

Fig. 9. Bode plot of (a) converter-side inductor current loop, (b) grid-side inductor current loop and (c) input voltage loop.

possible PI parameter is varying and very narrow in the selection range. Therefore, at the light load situation or low PV voltage situation, the system phase margin can't satisfy in the design under the same set of control parameters at the full load situation. Differently, once the damping factor is added, the resonance peak is reduced and a smooth phase change appears. Larger in the value of K_D, a smaller resonance peak amplitude can be obtained. Therefore, a stable system is able to be realized under the proposed control method.

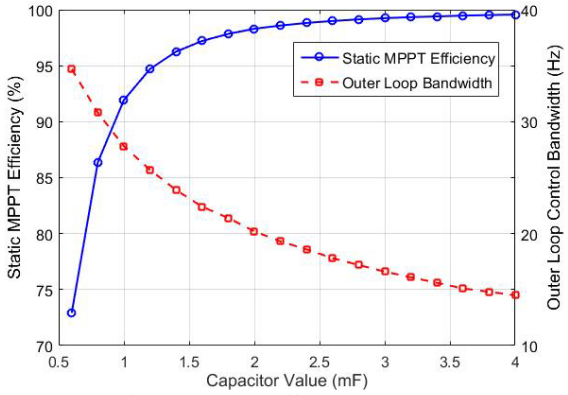

Fig. 10. System performance under different input capacitor values.

The Bode plot of the presented control methodology is shown in Fig. 9 where the converter-side inductor current loop, grid-side inductor current loop, and input voltage loop are plotted in Fig. 9 (a), (b) and (c) respectively. In the presented methodology, both converter-side inductor current and the grid-side inductor current are also under controlled separately. The converter-side inductor current loop is the fastest loop which controls the switching action of the converter. The input voltage loop is the lowest in response. The inner loop bandwidth is set to 5 to 10 times lower than the target switching frequency. Meanwhile, each loop bandwidth is also set to 5 to 10 times different from each other to avoid the loop inference. Also, the system phase margin keeps higher than 45 degrees and a positive phase margin is kept at all the test cases. The influence of irradiance change is demonstrated through the Bode plot diagram in Fig. 9. The influence is mainly reflected in the stability of the inner loop of the system, but it is not significant in other loops. As shown in Fig. 9 (a), when the irradiance is dropped, the phase margin for the inner loop is reduced and the resonant pole magnitude is increased. If the design margin and the damping factor are not enough, at the low irradiance situation, the phase margin may drop below 45 degrees and a positive magnitude appears in the resonant pole. Thus an unstable situation occurred. Under the proposed control scheme, all the loops are unaffected by the resonant issue and provide a stable inverter performance. Thus, stable system operation can be always guaranteed.

B. System MPPT Efficiency

The MPP tracking efficiency is used to indicate the relationship between the panel output power and the maximum available power from the panel. The system tracking performance is mainly depended on the input capacitor value and the loop bandwidth of the outer loop. Two different types of tracking efficiency are involved, which are static and dynamic MPPT efficiencies. According to [20], the formula of the static MPPT efficiency can be determined as,

$$\eta_{\text{static}} = \frac{1}{n \cdot P_{\text{peak}}} \cdot \left[\sum_{k=1}^{n} i_{\text{PV}}\left(\frac{k \cdot 2T}{n}\right) \cdot v_{\text{PV}}\left(\frac{k \cdot 2T}{n}\right)\right], \quad (19)$$

where P_{peak} is the maximum available power from the PV panels under a fixed irradiation situation.

Meanwhile, the formula of the dynamic MPPT efficiency is,

$$\eta_{\text{dynamic}} = \frac{\int_0^{T_s} i_{\text{PV}}(t) \cdot v_{\text{PV}}(t) dt}{\int_0^{T_s} p_{\text{peak}}(t) dt}, \quad (20)$$

where T_s is a dynamic period defined in [20] and p_{peak} is the offered maximum available power from the PV panels during the dynamic period.

V. Experimental Verification

A 750W grid-connected buck-boost type PV inverter (Manitoba Inverter) prototype, as shown in Fig. 11, has been implemented for system verification. A set of experimental results is shown in Fig. 12 and Fig. 13. In the evaluation, a solar array simulator, Chroma 62050H-600S, was applied as the inverter source. It used to simulate PV panels with series connection structures and voltages in the range of 200 Vdc. The output of the inverter was directly connecting to a 120 Vac grid.

Specification of the prototype and the key parameters of the simulator setup are given in TABLE I. Accordingly, the corresponding PV characteristic is shown in Fig. 14 (a) with the used of a P-V curve where the MPP is located at 100 Vdc. The corresponding MPP current is 7.5 A. Similarly when the MPP point is shifted 200 Vdc, another P-V curve is generated which is shown in Fig. 14 (b). The corresponding MPP current is 3.75 A. The output of the PV panel was in a non-linear characteristic. When the irradiation was 1000 W/m^2, the full rated power was expected to be 750 W.

TABLE I Specification of the PV Simulator at 100 Vdc with 1000 W/m2 and of the inverter prototype.

Simulator	Parameter	MPP Power	MPP Voltage	MPP Current	Open Circuit Voltage	Short Circuit Current
	Value	750 W	100 V	7.5 A	121.18 V	8.087 A
Prototype	Parameter	Grid Frequency	Grid Voltage	Switching Frequency	Inductors (L_1 & L_2)	Capacitor (C_{AB})
	Value	60 Hz	120 Vac	20 kHz	780 µH	5.6 µF

In Fig. 12 (a), a steady state performance is demonstrated under 1000W/m^2 irradiation and with 100 Vdc input. Under the presented control methodology, the system was stabilized at the MPP voltage point. Also, a continuous and sinusoidal grid current was resultant. According to the inverter operation principle, both inductor currents were different in each half line cycle. In the positive half line cycle, L_1 acted as the converter-side inductor which was used for the power conversion. In the negative half line cycle, L_1 acted as the grid-side inductor which was used to filter the HF grid current ripple. As a result, the shape and the magnitude of i_{L1} were different in each half line cycle. Meanwhile, in Fig. 12 (b), it shows the importance of the damping circuit. When the damping coefficient was dropped to 0.002, the inner loop stability was affected. As mentioned in Section IV, when the damping coefficient was not enough, the magnitude gain at the resonance point became positive. Thus, the system stability was affected. Other than 100 Vdc MPP voltage, the inverter also performed stable at different input voltage points. In Fig. 13, the steady state waveform of the inverter are demonstrated at 200 Vdc input, respectively. Stable system performance was obtained and a sinusoidal grid current was achieved. From the test results, they showed that all targeted control objectives were met and there were no unstable situations.

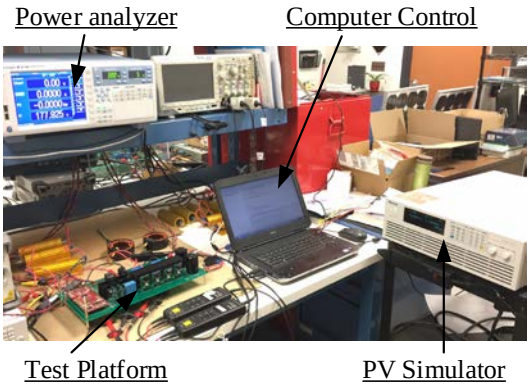

Fig. 11. Experimental test setup.

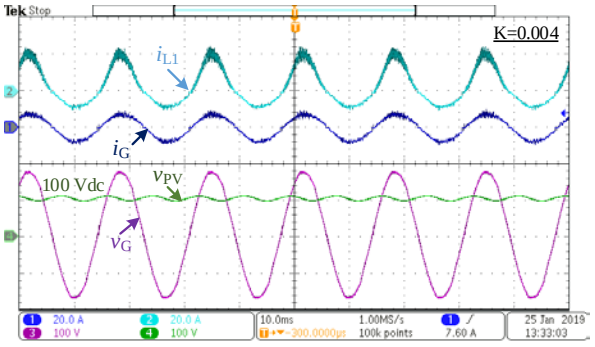

(a)

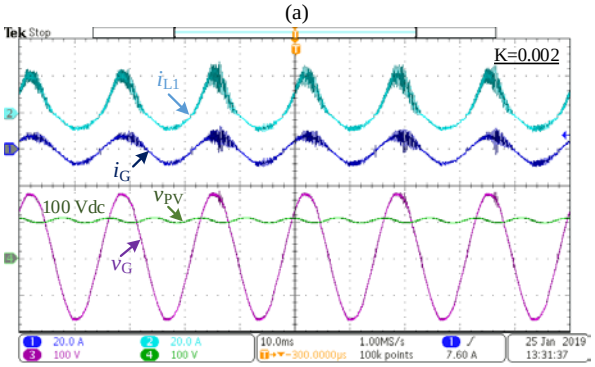

(b)

Fig. 12. Steady state waveform at 100 Vdc PV input and 1000 W/m^2 with a, (a) 0.004 and (b) 0.002 damping coefficients.

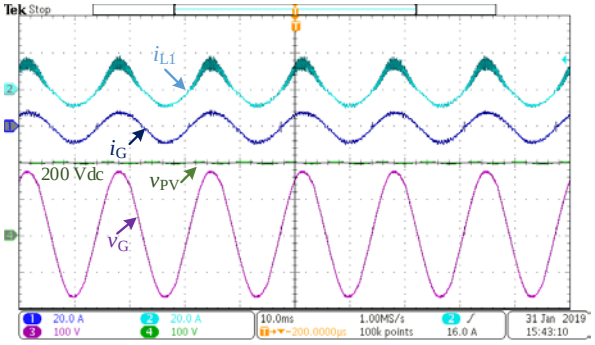

Fig. 13. Steady state waveform at 1000 W/m^2 with 200 Vdc PV input.

TABLE II Summary table of the system MPPT efficiencies.

MPP Voltage (Vdc)	Static MPPT Efficiency (%)	Dynamic MPPT Efficiency (%)
100	98.5	98.1
200	99.9	99.4

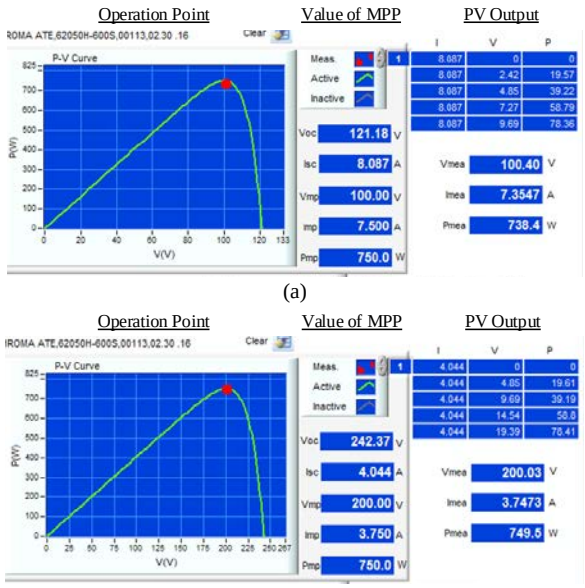

Fig. 14. PV characteristic, (a) at 100 Vdc and (b) 200 Vdc PV input.

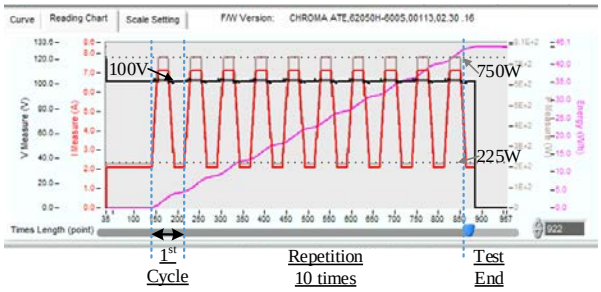

Fig. 15. Dynamic MPPT test under EN50530 with 100 Vdc PV input.

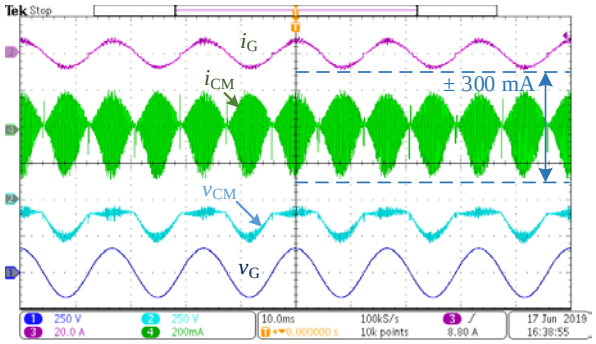

Fig. 16. Leakage current measurement at 1000 W/m^2 with 100 Vdc PV input.

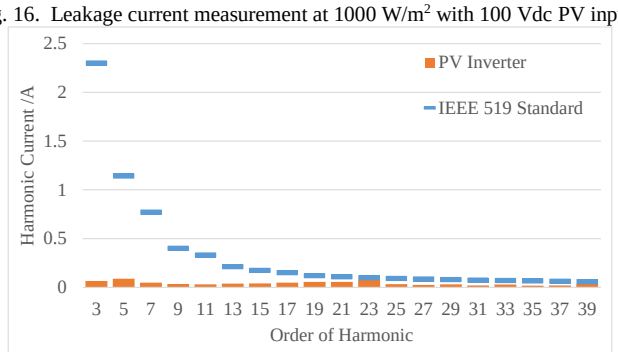

Fig. 17. Output current harmonic spectrum at 1000 W/m^2 with 100 Vdc PV input.

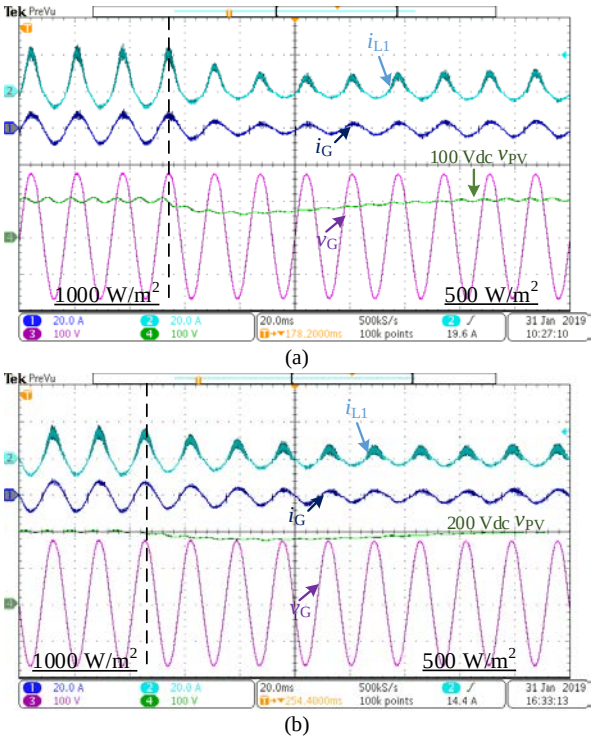

Fig. 18. Waveform of transient operation from 1000 W/m^2 to 500 W/m^2 at (a) 100 Vdc and (b) 200 Vdc PV inputs.

The function of the MPPT is shown in Fig. 14. During the steady state, the system was able to stabilize at the MPP voltage point and to collect the maximum available power from the PV panel. During the tracking, when the system voltage fell in the left part of the MPP voltage point, the reference voltage would be increased to track back the MPP. In contrast, the reference voltage would also be reduced when the system voltage fell in the right part of the MPP voltage point according to the implemented tracking function. As shown in Fig. 14 (a), the system static MPPT efficiency at 100 Vdc MPP voltage is kept higher than 98.5 %. According to EN50530 [20], a dynamic sequence was applied to the PV simulator through the programming software. The dynamic MPPT test pattern and the 100 Vdc test result are shown in Fig. 15. From the simulator, the measured system dynamic MPPT efficiency was 98.1%. Similarly, at 200 Vdc MPP voltage test case, both dynamic and static MPPT efficiencies were measured and both were kept higher than 99.4%. A summarized table of the system MPPT efficiencies is given in TABLE II. As a result, an efficient PV inverter system is able to be guaranteed.

In the designed inverter, the highest inductor current peak appeared at 1000 W/m^2 with 100 Vdc PV input voltage, and the current amplitude between the converter-side and the grid-side inductors was the largest. That was also the maximum leakage current point of the platform. Accordingly, the corresponding leakage current performance is measured and is shown in Fig. 16, where a 100 nF capacitor is added into the system to simulate the effect of the parasitic capacitor. The connection method was with the same structure as shown in Fig. 3. The voltage between the Neutral of the grid and the negative bus voltage was measured and used to represent the common mode (CM) noise voltage of the system. The current that flowed

through the parasitic capacitor was defined as the leakage current. From the result, it shows that the high frequency ripple on the CM noise voltage was maintained in a relatively small value and a low leakage current was resultant. In the design, the resultant leakage current was always kept within the 300 mA range, which was accepted by the industrial requirement [21]. Thus, a low leakage current performance was guaranteed in this inverter design. Meanwhile, under the proposed control scheme, the system power factor always maintained higher than 0.98. All the time, the grid current THD was within 5% under IEEE 519 [22]. The current harmonic spectrum of Fig. 14 (a) is shown in Fig. 17 and the corresponding current THD was 4.22%. The IEEE 519 class A standard requirement was applied and all the sub-harmonic contents were under the corresponding limitation line. Thus, a high power quality system was proved.

In Fig. 18, a set of transient waveforms of the presented system is demonstrated. In Fig. 18 (a), the MPP voltage was fixed at 100 Vdc, the irradiation was dropped from 1000 W/m^2 to 500 W/m^2. From the result, it showed that after a step change in irradiation, the system was able to recover back to the MPP in a short period of time and to maintain a stable performance during the transient process. The response time was mainly depending on the size of the input capacitor and the tracking speed of the outer loop. Similarly, in Fig. 18 (b), the irradiation was dropped from 1000 W/m^2 to 500 W/m^2 at 200 Vdc. From the result, it showed that after a step change in irradiation, the system was also maintained a stable performance during the transient process. Moreover, the system was recovered to the MPP in a short period of time and the new MPP voltage was tracked correctly. In both test cases, it took around 120 ms to track back the MPP, in which the tracking speed was limited by the bandwidth of the voltage control loop and the size of the input capacitor. Under the proposed control scheme, it offered a high quality output current to the grid, kept tracking the MPP at the input and let the inverter to operate stably in any situation. Thus, the advantages of the inverter topology are maximized in PV applications.

VI. Conclusions

The paper has presented a comprehensive control strategy for a recently proposed single-phase single-stage transformerless buck-boost type PV inverter system. The system design and the detailed system modelling were given in this paper. Under the proposed control scheme, the PV inverter was able to effectively transfer the maximum available solar power into the grid, maintained the system grid current in high quality. Also, such proposed control scheme improved the system stability and let the system able to adopt all the possible outputs from the PV panel. The performance of the PV inverter system and control methodology were demonstrated with the experimental results. A 750W grid-connected PV prototype has been implemented. Stable performance was able to be obtained in both steady state conditions and transient responses. All the experimental results were consistent with the theoretical concepts.

References

[1] K. K. M. Siu and C. N. M. Ho, "Modelling and Stability Study of a Single Stage Buck-Boost Inverter for PV Application," *Proc. IEEE ECCE*, pp. 7088- 7093, Sept. 2018.

[2] T.K.S. Freddy, N.A. Rahim, W.P. Hew, and H.S. Che, "Comparison and Analysis of Single-Phase Transformerless Grid-Connected PV Inverters," I*EEE Trans. Power Electron.*, vol. 29, no.10, pp.5358 – 5369, Oct. 2014.

[3] S.B. Kjaer, J.K. Pedersen, and F. Blaabjerg, "A review of single-phase grid-connected inverters for photovoltaic modules," *IEEE Trans. Ind. Appl*., vol.41, no.5, pp.1292-1306, Oct. 2005.

[4] S. Jain and V. Agarwal, "A Single-Stage Grid Connected Inverter Topology for Solar PV Systems With Maximum Power Point Tracking," *IEEE Trans. Power Electron.*, vol. 22, no. 5, pp.1928 – 1940, Sept. 2007.

[5] H. Patel and V. Agarwal, "A single-stage single-phase transformer-less doubly grounded grid-connected PV interface," *IEEE Trans. Power Electron.*, vol. 24, no. 1, pp. 93–101, Mar. 2009.

[6] T. Sreekanth, N. Lakshminarasamma and M. K. Mishra, "A Single-Stage Grid-Connected High Gain Buck–Boost Inverter With Maximum Power Point Tracking," *IEEE Trans. Energy Convers.*, vol. 32, no. 1, pp. 330-339, Mar. 2017.

[7] C. N. M. Ho and K. K. M. Siu, "Manitoba Inverter - Single Phase Single-Stage Buck-Boost VSI Topology," *IEEE Trans. Power Electron.*, Early Access.

[8] M. Jang, M. Ciobotaru and V. G. Agelidis, "A Single-Stage Fuel Cell Energy System Based on a Buck--Boost Inverter with a Backup Energy Storage Unit," *IEEE Trans. Power Electron.*, vol. 27, no. 6, pp. 2825-2834, June 2012.

[9] P. Sanchis, A. Ursua, E. Gubia and L. Marroyo, "Design and experimental operation of a control strategy for the buck-boost DC-AC Inverter," *Proc. IEEE Electric Power Applications*, vol. 152, no. 3, pp. 660-668, 6 May 2005.

[10] X. Ji, T. Zhang, H. Su, Z. Xia, Z. Tang and G. Zhu, "Single phase gird connected inverter based on one-cycle current control," *Proc. IEEE IPEMC-ECCE Asia*, pp. 2899-2903, May 2016.

[11] B. Zhao, R. Ma, B. Liang and A. Abramovitz, "One-cycle-controlled high gain single stage Buck-Boost inverter for photovoltaic application," *Proc. IEEE IECON, pp*. 7813-7817, Nov. 2017.

[12] A. Darwish, A. Massoud, D. Holliday, S. Ahmed and B. Williams, "Generation, performance evaluation and control design of single-phase differential-mode buck–boost current-source inverters," *IET Renewable Power Generation*, vol. 10, no. 7, pp. 916-927, July 2016.

[13] Z. Yue, "Study of buck-boost photovoltaic inverter based on discrete sliding mode control strategy," *Proc. IEEE MACE*, pp. 1643-1647, July 2011.

[14] Y. He, K. W. Wang, and H. S. H. Chung, "Utilization of Proportional Filter Capacitor Voltage Feedforward to Realize Active Damping for Digitally Controlled Grid-Tied Inverter Operating Under Wide Grid Impedance Variation," *Proc. IEEE ECCE*, pp. 4450 – 4457, Sept. 2014.

[15] H. Patel and V. Agarwal, "MPPT Scheme for a PV-Fed Single-Phase Single-Stage Grid-Connected Inverter Operating in CCM With Only One Current Sensor," *IEEE Trans. Energy Convers.*, vol.24, no.1, pp. 256 – 263, Mar. 2014.

[16] F.E. Aamri, H. Maker, D. Sera, S. Spataru, J.M. Guerrero, and A. Mouhsen, "A Direct Maximum Power Point Tracking Method for Single-Phase Grid Connected PV Inverters," *IEEE Trans. Power Electron.*, Early Accepted.

[17] A.Gow, and C. D. Manning, "Development of a photovoltaic array model for use in power electronics simulation studies," *IEEE Proc. Elect. Power Appl.*, vol. 146, no. 2, pp. 193-200, 1999.

[18] J. Cubas, S. Pindado, C.D. Manuel, C. "Explicit Expressions for Solar Panel Equivalent Circuit Parameters Based on Analytical Formulation and the Lambert W-Function," *Energies*, vol. 7, pp. 4098–4115, Jun. 2014.

[19] M. Fazeli, J.B. Ekanayake, P.M. Holland, and P. Igic, "Exploiting PV Inverters to Support Local Voltage—A Small-Signal Model," *IEEE Trans. Energy Convers.*, vol.29, no.2, pp. 453 – 462, Jun. 2014.

[20] *Overall efficiency of grid connected photovoltaic inverters*, EN Standard 50530, 2010.

[21] *Safety of Power Converters for Use in Photovoltaic Power Systems—Part 1: General Requirement*, IEC Standard 62109-1-2007, 2007.

[22] *IEEE Recommended Practice and Requirements for Harmonic Control in Electric Power Systems*, IEEE 519-2014, 2014.